Complex Oxide-metal Hybrid Metamaterials with Integrated Magnetic and Plasmonic Non-noble Metal Nanostructures

Jijie Huang, Bin Zhang, Danny Hermawan, Alfredo Sanjuan, Benson Kunhung Tsai, Jialong Huang, R. Edwin Garcıá, and Haiyan Wang**

Vertically aligned nanocomposite (VAN) thin films offer exceptional physical properties through diverse material combinations, providing a robust platform for designing complex nanocomposites with tailored performance. Considering materials compatibility issues, most of oxide-metal VANs have focused on noble metals as the secondary phase in the oxide matrix. Here, an oxide-metal hybrid metamaterials in the VAN form has been designed which combines ferroelectric $BaTiO_3$ (BTO) with two immiscible non-noble metal elements of Co and Cu, resulting in a three-phase BTO-Co-Cu (BTO-CC) VAN film. This film exhibits a characteristic nanopillar-in-matrix nanostructure with three distinct types of nanopillar morphologies, i.e., Co-rich cylindrical nanopillars, Cu-Co-nanolaminated Co rectangular nanopillars and Co-Cu-core–shell cylindrical nanopillars. Phase field modeling indicates the constructed structure is resulted from the interplay between thermochemical, chemomechanical, and interfacial energy driving forces. The strong structural anisotropy leads to anisotropic optical and magnetic properties, presenting potential as hyperbolic metamaterial (HMM) with transverse-positive dispersion in the near-infrared region. The inclusion of non-noble Cu nanostructure induces surface plasmon resonance (SPR) in the visible region. Additionally, ferroelectric properties have been demonstrated in a BTO/BTO-CC bilayer, confirming room-temperature multiferroicity in the film. The complex three-phase VANs offer a novel platform for exploring electro-magneto-optical coupling along vertical interfaces toward future integrated devices.

1. Introduction

Vertically aligned nanocomposite (VAN) thin films are an emerging class of nanostructured materials that exhibit exceptional multifunctional properties owing to their unique vertical architecture, which provides a large vertical interfacial area between the two phases, facilitating enhanced charge transfer, ion diffusion, strain engineering, magneto-optical coupling, etc.[1–5] The VAN morphology enables the combination of distinct properties from each constituent material, leading to enhanced or entirely new functionalities that could not be easily achieved in single-phase materials. In addition, the ability to precisely control the composition, orientation, size, and density of the secondary nanostructures, further enables the customization of VAN thin films to meet specific application requirements, positioning them at the forefront of multi-functional materials development.[6–10] Furthermore, the material selection of the VAN thin films has been extended beyond the typical oxide-oxide ones, such as oxide-metal, nitride-metal, oxide-nitride, and selenide-metal[11–13] which provides great opportunities to achieve specific properties through VAN system design.

To further discover the potential of the functional VAN thin films, recently, multi-phase VAN (MP-VAN) systems have been explored, such as all-oxide systems,[14,15] oxide-metal alloy systems[16,17] nitride-metal alloy systems,[18] oxide-oxide-metal systems[19] and nitride-oxide-metal systems.[20] The MP-VANs exhibit exceptional physical properties that are unattainable in traditional single-phase thin films. For example, a notable self-biased magnetoelectric effect at room temperature has been

---

J. Huang, B. Zhang
School of Materials
Shenzhen Campus of Sun Yat-sen University
Shenzhen 518107, China
E-mail: huangjj83@mail.sysu.edu.cn

The ORCID identification number(s) for the author(s) of this article can be found under https://doi.org/10.1002/adfm.202500741

DOI: 10.1002/adfm.202500741

D. Hermawan, A. Sanjuan, B. K. Tsai, J. Huang, R. E. Garcıá, H. Wang
School of Materials Engineering
Purdue University
West Lafayette, IN 47907, USA
E-mail: hwang00@purdue.edu

H. Wang
School of Electrical and Computer Engineering
Purdue University
West Lafayette, IN 47907, USA

obtained in a three-phase nanocomposite thin film, which comprises ferrimagnetic $NiFe_2O_4$ nanocolumns coated with antiferromagnetic p-type NiO embedded in ferroelectric $Na_{0.5}Bi_{0.5}TiO_3$ matrix.[15] The multi-phase nature of the MP-VAN thin films allows for the exploitation of the distinct characteristics of each material, resulting in enhanced or novel functionalities that surpass those of single-phase systems.

Of particular interest are the oxide-metal or oxide-alloy systems combining oxides with one or more metal species, harnessing the functionalities of both components to yield remarkable magnetic, electrical, and optical properties. Various two-phase oxide-metal systems have been developed, including Au-$La_{0.67}Sr_{0.33}MnO_3$,[8] Ni-CeO_2,[21] Co-$BaZrO_3$,[9] Au-HfO_2,[22] Ni-$SrTiO_3$,[23] Cu-ZnO,[24] etc., while less efforts have been devoted to develop multi-phase oxide-metal alloy systems.[16,17,25,26] The metals typically incorporated into these systems include precious metals such as Au and Ag, known for their surface plasmon resonance (SPR), as well as ferromagnetic metals like Co, Ni, and Fe. Cu has rarely been incorporated into the MP-VAN systems, despite the fact that Cu is an earth-abundant low-cost metal compared to the precious metals and it also exhibits intense and tunable localized SPR across the ultraviolet-visible to the near-infrared region.[27,28]

In this work, a new three-phase VAN system composed of ferroelectric $BaTiO_3$ (BTO) with two non-noble metals, i.e., plasmonic Cu and ferromagnetic Co (BTO-CuCo, denoted as BTO-CC) has been developed and fabricated using a mixed composite target with the molar ratio of BTO:Cu:Co = 0.5:0.25:0.25. In selecting the oxide matrix, beyond the BTO utilized in this study, other oxides such as $BaZrO_3$ and CeO_2 can also be employed. The key criteria for these oxides are immiscibility with the metal phases and excellent lattice matching, which are essential for optimizing the structural coherence and introducing multifunctional properties of the composite films. The microstructure of the film was meticulously characterized. Comprehensive investigations on its physical properties, including magnetic performance and optical response, were conducted. Furthermore, a BTO-capped BTO-CC sample was deposited to explore the ferroelectric properties of the film, demonstrating promising potential as a room-temperature multiferroic material. The successful synthesis of the BTO-CC nanocomposite thin film highlights the feasibility of designing new oxide-alloy MP-VANs incorporating different non-noble metal species, thereby expanding avenues for achieving tailored physical properties.

2. Results and Discussion

The microstructure of the BTO-CC nanocomposite thin film was first characterized by scanning transmission electron microscopy (STEM), in both cross-sectional and plan-view directions. **Figure 1a1** shows a low-magnification cross-sectional STEM image with corresponding energy-dispersive X-ray spectroscopy (EDS) image in Figure 1a2. A typical VAN structure of nanopillars-in-matrix was observed, with the thickness of the film to be ≈98 nm. High-resolution high angle annular dark field (HAADF) STEM imaging was applied on selected area to reveal a typical nanopillar (NP) in atomic scale, as shown in Figure 1b1. The image indicates the high crystallinity of the film with nearly perfect lattice structure across the pillar and the BTO matrix. Its corresponding filtered inverse fast Fourier transform (FFT) image in Figure 1b2 reveals that there are obvious lattice distortions at the vertical oxide/metal interfaces.

Plan-view STEM image, along with corresponding EDS mapping results, further elucidates the microstructure and composition distribution of the nanopillars, as shown in Figure 1c1,2, respectively. Interestingly, three types of NPs were identified: one with primary Co-rich pillars (NP1), the second exhibiting a novel sandwiched structure with Co being sandwiched in between two Cu nanoplates (NP2), and the third with Co-Cu core–shell structures (NP3). The HAADF STEM image and the corresponding filtered inverse FFT image in Figure 1d1,d2 respectively, reinforce the high epitaxial quality of the BTO-CC films with obvious lattice distortions in the BTO matrix near the nanopillars. The lattice-mismatch induced strain is confined to the oxide-metal interface region, as shown in the plan-view geometric phase analysis (GPA) ε_{yy} (in-plane strain) map in Figure S1 (Supporting Information), which presents in-plane compressive strain in BTO and tensile strain in the metal phases at the interface. Most of the BTO lattices are clean and strain-free. Nanopillars in the NP1 type appear to be cylindrical-shaped ones, with the lattice relationships of Co[100]/BTO[100], Co[010]/BTO[010], as shown in Figure 1e1. EDS mapping in Figure 1e2 confirms the presence of primarily Co and very minute Cu in NP1. Meanwhile, the pillars in the NP2 type displays a nearly rectangular prism morphology with Co sandwiched by two Cu nanoplates, as shown in the HAADF STEM image in Figure 1f1 and corresponding EDS mapping in Figure 1f2. The lattice structure for NP2 is determined as CoCu[110]/BTO[100], CoCu[-110]/BTO[010]. NP3 presents a unique Co-Cu core–shell structure with Co core and Cu shell. There are 4–5 NP3 type nanopillars in Figure 1c2 showing such core–shell structure. A low magnification STEM image over a large area in Figure S2 (Supporting Information) demonstrates the uniform distribution of metal NPs within the oxide matrix, allowing the overall structure to be schematically constructed as shown in Figure 1g. The standard θ-2θ X-ray diffraction (XRD) pattern of the BTO-CC film, displayed in Figure S3 (Supporting Information), reveals only BTO (00*l*) peaks. The *c* lattice parameter is estimated to be 4.101 Å, indicating an out-of-plane tensile strain of 1.74% in the BTO phase. Such strain could be due to the large c-lattice parameter of the Co nanopillars (d_{Co} = 0.401nm). It is noted that the peaks for metal NPs are very small or nearly invisible. This could be related to the very small pillar size of the NPs. As evidenced in the high-resolution TEM study on these samples, the lattice of the metal NPs are clearly visible with high crystallinity. Overall, the BTO-metal interface is relatively sharp, while weak interdiffusion might occur over a few atomic planes, as revealed by the atomic-scale electron energy-loss spectroscopy (EELS) study in STO-Ni VAN system.[29] The BTO/metal bonding (BTO/Cu and BTO-Co) is complex, previous studies indicate weaker BTO/Cu and stronger BTO/Co bonding might exist owing to lower and higher affinity for oxygen of Cu and Co, respectively.[30,31] Regarding the energy bands at the interface, the conduction band minimum (CBM) and valence band maximum (VBM) of BTO are ≈3.3 and ≈0 eV, with a work function of ≈3.9–4.4 eV, while Cu and Co obtain work function of 4.7 and 5.0 eV, respectively. Therefore, both the BTO/Cu and BTO/Co heterointerface form Schottky contact. The atomic structure at the BTO/metal interface is interesting however such interfacial

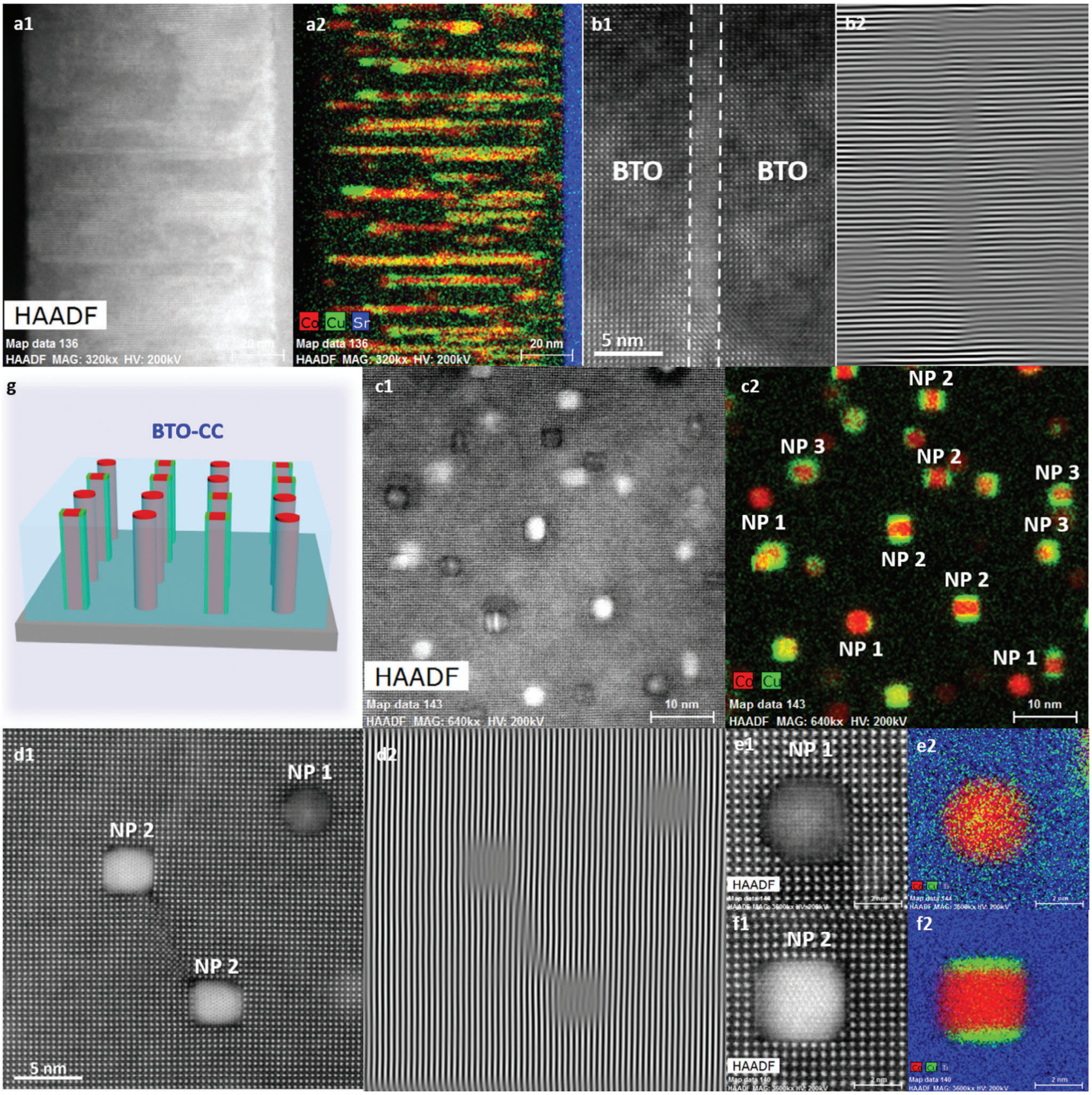

Figure 1. Detailed microstructure of the BTO-CC nanocomposite thin film. a1) Cross-sectional STEM image with a2) corresponding EDS mapping; b1) High-resolution STEM image of selected area with (b2) corresponding masked inverse FFT image; c1) Plan-view STEM image with c2) corresponding EDS mapping; d1) High-resolution STEM image of selected area with d2) corresponding masked inverse FFT image; HAADF STEM images of e1) type-1 and f1) type-2 nanopillars with corresponding EDS mapping in e2) and f2), respectively; g) Schematic illustration of the BTO-CC film.

analysis is very challenging due to the ultra-fine metal NPs. Thus future investigations are needed to reveal the bonding structures at the BTO-metal interfaces.

To investigate the optical response of the BTO-CC film, the transmittance spectrum (300–1800 nm) was characterized, as shown in **Figure** 2a. The spectrum reveals two notable features: a narrow valley at 505 nm and a broad valley at 756 nm, which are attributed to SPR from the metal nanostructures. Both Cu and Co are considered to have SPR effect,[32,33] and the extinction band wavelength highly relies on the nanostructure size, shape, chemical nature and local dielectric environment.[34] The SPR characteristics are further confirmed by the COMSOL simulated optical field enhancement maps at 505 and 750 nm shown in Figure 2b and Figure S4 (Supporting Information), respectively. These mappings indicate that the pronounced plasmonic features are primarily due to the Cu nanoshells and the Cu/Co

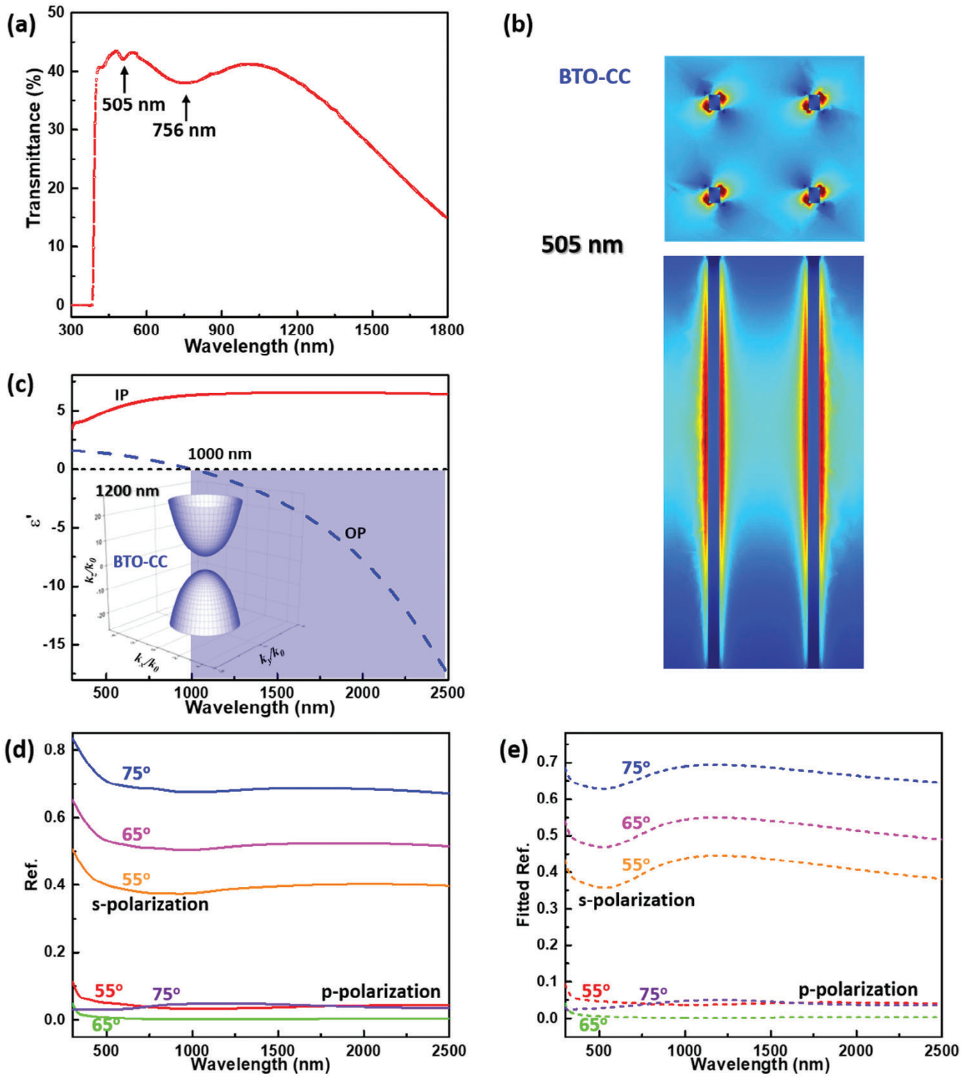

Figure 2. Optical properties of the BTO-CC film. a) Transmittance spectrum measured from 300 to 1800 nm; b) COMSOL simulated optical field enhancement maps corresponding to incident illumination at 505 nm in both in-plane (upper panel) and out-of-plane (lower panel) view directions; c) Real part of complex dielectric function (ε′), inset shows the extracted iso-frequency surfaces at 1200 nm; d) Experimental and e) simulated reflectivity spectra at different angles of incidence for *p*-polarized and *s*-polarized incident light.

interfaces. Additionally, the hybridization of nanostructures in close proximity contributes to the overall SPR effect.

The anisotropic nature of the dielectric-metal VAN structure of the BTO-CC film offers an excellent platform for achieving anisotropic physical properties. To explore the optical anisotropy, angular-dependent ellipsometry measurements have been conducted. The ellipsometric phi (φ) values, measured over the range of 300 to 2500 nm, are presented in Figure S5 (Supporting Information). A uniaxial model is applied to derive the optical complex dielectric functions of the film in both IP (in-plane, i.e., parallel to the film surface) and OP (out-of-plane, i.e., perpendicular to the film surface) directions, as shown in Figure 2c and Figure S6 (Supporting Information) for the real part ε′ and imaginary part ε″, respectively. Real (n) and imaginary (k) part of effective refractive index of the BTO-CC film are also derived and presented in Figure S7 (Supporting Information). The results indicate that ε'_{IP} keeps positive across the entire measured wavelength, while ε'_{OP} becomes negative from 1000 nm onward, demonstrating the film's potential as a hyperbolic metamaterial (HMM) with transverse-positive dispersion in the near-infrared region. To probe the optical iso-frequency surface of the film, its electromagnetic wave (k-wavevector) dispersion relation is given by: $\frac{k_x^2+k_y^2}{\varepsilon_\perp}+\frac{k_z^2}{\varepsilon_\parallel}=\frac{\omega^2}{c^2}=k_0^2$, where k_x, k_y and k_z are the wave vector components in[100],[010] and[001] directions, respectively; x and c are the frequency and speed of light, respectively. The hyperbola with two sheets shown in the inset of Figure 2c indicates the Type-I hyperbolic metamaterial. Optical anisotropy was further demonstrated through angular dependent and polarization-resolved reflectivity measurement at incident angles of 55°, 65° and 75°, as shown in Figure 2d,e are the measured and simulated results. The fitted and measured reflectivity results align well

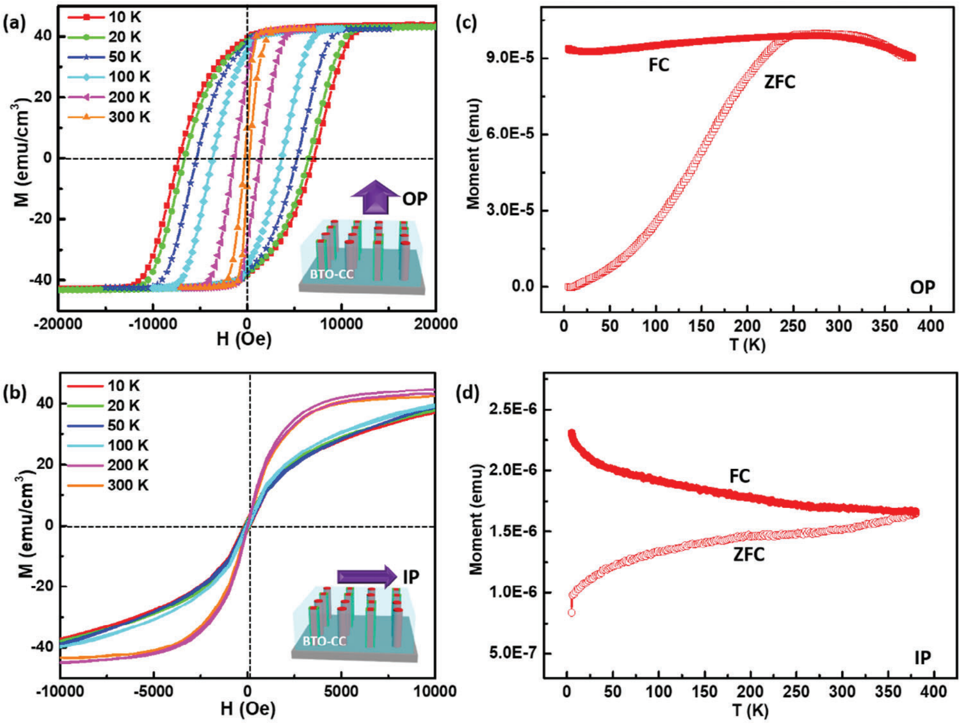

Figure 3. Magnetic properties of the BTO-CC film. Magnetic hysteresis loops measured at different temperatures under a) Out-of-plane, OP or b) In-plane, IP external magnetic field; Magnetization-temperature (5–380 K) curves with the applied field in c) OP or d) IP directions.

across the entire wavelength range. The results also show that reflectivity increases with rising incident angles when s-polarized light strikes the film surface, consistent with classical electromagnetic theory.[35] Overall, the BTO-CC film exhibits intriguing optical properties, including SPR in the visible region, HMM behavior in the near-infrared region, and anisotropic optical responses, which indicates its potential applications in subwavelength imaging and hyperlens.

We then focus on the magnetic response of the BTO-CC nanocomposite thin film. Magnetic hysteresis (M-H) loops at different temperatures (10, 20, 50, 100, 200, 300 K) were measured under OP and IP magnetic fields, as shown in **Figure** 3a,b, respectively. The saturation magnetization (M_S) of the film could be estimated to be ≈43.5 emu cm^{-3} (note that the volume of the entire film is accounted), while the coercivity (H_C) decreases with increasing temperature due to the thermally activated magnetization reversal process (the temperature-dependent H_C is summarized in Table S1, Supporting Information). The OP and IP MH loops exhibit distinctly different shapes at all measured temperatures, indicating the magnetic anisotropy of the film. The magnetic anisotropy of the metal NPs arises from three factors: i). shape anisotropy; ii). interpillar magnetostatic dipole interaction and iii). magneto-crystalline anisotropy. These factors contribute to the total effective anisotropy field H_K, defined as $H_K = 2\pi M_S - 6.3\pi M_S r^2 L d^{-3} + H_{MC}$.[36] Where M_S is the saturation magnetization, L and r are the length and radius of the nanopillars, and d is the interpillar distance. Note that the magneto-crystalline anisotropy is negligible in magnetic nanowires. In this case, L, r, and d are estimated to be ≈100, ≈2.5, and ≈15 nm, respectively, based on the TEM/STEM results presented above. This results in a positive value of H_K, indicating the dominate factor of shape anisotropy.

Magnetization-temperature (M-T) measurements under zero-field cooling (ZFC) or 100 Oe field cooling (FC) have also been conducted to further investigate the magnetic properties, as depicted in Figure 3c,d are for OP and IP directions, respectively. In the OP direction, the ZFC curve shows an increase in magnetization with increasing temperature until reaching the blocking temperature (T_B) at ≈270 K, after which the magnetization begins to decrease. Below T_B, the magnetic anisotropy energy exceeds the thermal energy, thus preventing the magnetic moments from aligning with a small magnetic field. The FC curve is nearly flat below T_B, suggesting spin-glass-like behavior. This behavior likely results from non-negligible dipole–dipole interactions between the magnetic NPs. On the other hand, the FC and ZFC curves in the IP direction display a markedly different trend. The ZFC curve shows a monotonically increasing magnetization with increasing temperature, indicating that T_B is higher than 380 K. In this case, the easy axis for the NPs is along their length. When the NPs are warmed up in the presence of an external field, they acquire sufficient thermal energy to switch their magnetizations from the easy axes to the direction of the applied field. This results in an overall increase in the magnetization of the sample, as observed in the ZFC curve. These M-T results further confirm the magnetic anisotropy of the BTO-CC nanocomposite thin film. In addition, the ultra-fine size and high density of the metal NPs suggest the potential application in magnetic data storage with an estimated density as high as 5.3 TB in^{-2} in this case.

As BTO is a well-known ferroelectric material, and its coupling with magnetic NPs can potentially induce multiferroicity.

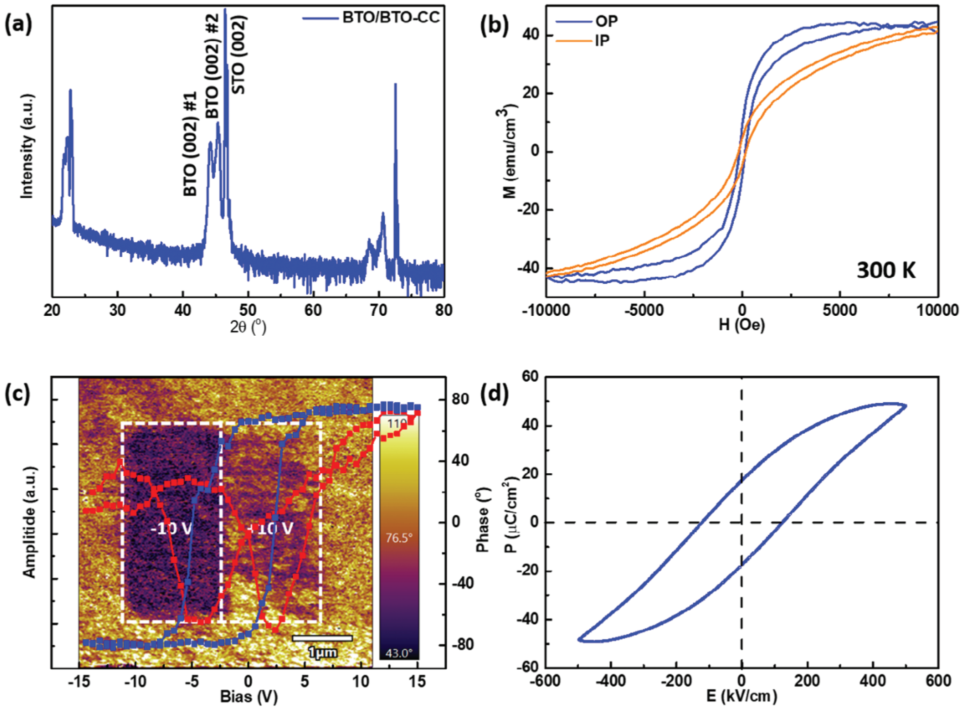

Figure 4. Properties of the BTO/BTO-CC bilayer film. a) Standard θ-2θ XRD pattern; b) M–H curves under IP and OP magnetic fields; c) Butterfly-like displacement-voltage (D-V) loop and the hysteresis phase-voltage loop, inset is the phase switching map; (d) P–E loop.

However, in the BTO-CC film, the conductive metal NPs hinder the application of an external electric field, thus an additional BTO top layer was deposited to form a BTO/BTO-CC bilayer on Nb-STO for the ferroelectric measurement. θ–2θ XRD measurement was first performed on the bilayer, as illustrated in **Figure 4a**. Two sets of BTO (00l) peaks are determined, which correspond to the top BTO layer and the BTO phase within the BTO-CC layer. The c lattice parameters are determined to be 4.094 and 3.992 Å, producing a tensile strain of 1.56% and a compressive strain of -0.97%, for the BTO phase in BTO-CC layer and top BTO layer, respectively. Additionally, the room-temperature M–H curves in both IP and OP directions confirm the ferromagnetic property of the bilayer film, as depicted in Figure 4b.

To explore the ferroelectric performance, Au top electrodes with 100 μm diameter were deposited, and the conductive Nb-STO was used as the bottom electrode. Piezoelectric force microscopy (PFM) was carried out by applying DC biases of -10 and +10 V on two adjacent domains, which resulted in the out-of-plane domain switching evidenced by the distinct color contrast observed in the phase and amplitude switching maps in Figure 4c and Figure S8 (Supporting Information), respectively. Note that the NPs could hardly be observed in the PFM image due to their small size and conducting nature. The local ferroelectricity of the film has been further confirmed by the characteristic butterfly-shaped displacement-voltage (D-V) loop and the hysteresis phase-voltage loop with a sharp 180° change in Figure 4c. Lastly, the polarization-electric field (P-E) loop has been characterized to assess the overall ferroelectricity of the entire film. As shown in Figure 4d, the hysteresis loop reveals a saturation polarization (P_s) of 49.4 μC cm^{-2}, remnant polarization (P_r) of 17.6 μC cm$^{-2,}$ and coercive field (E_c) of ≈120 kV cm^{-1}. It is worth noting that the ferroelectricity results from both the top BTO layer, in addition to the BTO in the nanocomposite layer. Furthermore, since the nanocomposite film was deposited under vacuum conditions, the presence of oxygen vacancies in the BTO matrix is inevitable. These oxygen vacancies could act as charge trap sites, potentially increasing leakage current and degrading the overall ferroelectric properties of the films. The combined magnetic and ferroelectric properties of the BTO/BTO-CC bilayer underscore its potential as a room-temperature multiferroic system, which allows the potential applications in actuators, switches, magnetic field sensors, etc.

Comparing the BTO-CC VAN system to the previous BTO-based VAN systems, there are several unique characteristics. First, both Cu and Co are non-noble metals and both can grow heteroepitaxial nanopillars in the BTO matrix without obvious chemical interaction with the matrix. Compared to Au and Ag which are widely used noble metals in VAN designs[12,13,19,22,26] because of their chemical inertness, the successful implementation of multielement of non-noble metals as VAN nanopillars presents enormous metal selections toward other unique functionalities. Second, the very unique sandwiched structure of Cu/Co/Cu nanopillars is structurally interesting. Such in-plane anisotropic could be related to the anisotropic interface structures based on the unique in-plane orientation relationship. As above discussed, the orientation between Co-Cu nanopillars and the BTO matrix is CoCu[110]/BTO[100], CoCu[-110]/BTO[010]. This results in two uniquely different interfaces with different surface energy, which could be the main reasons for the observed three types of nanostructures. We thus have conducted the phase field modeling to examine the underlying mechanisms for such

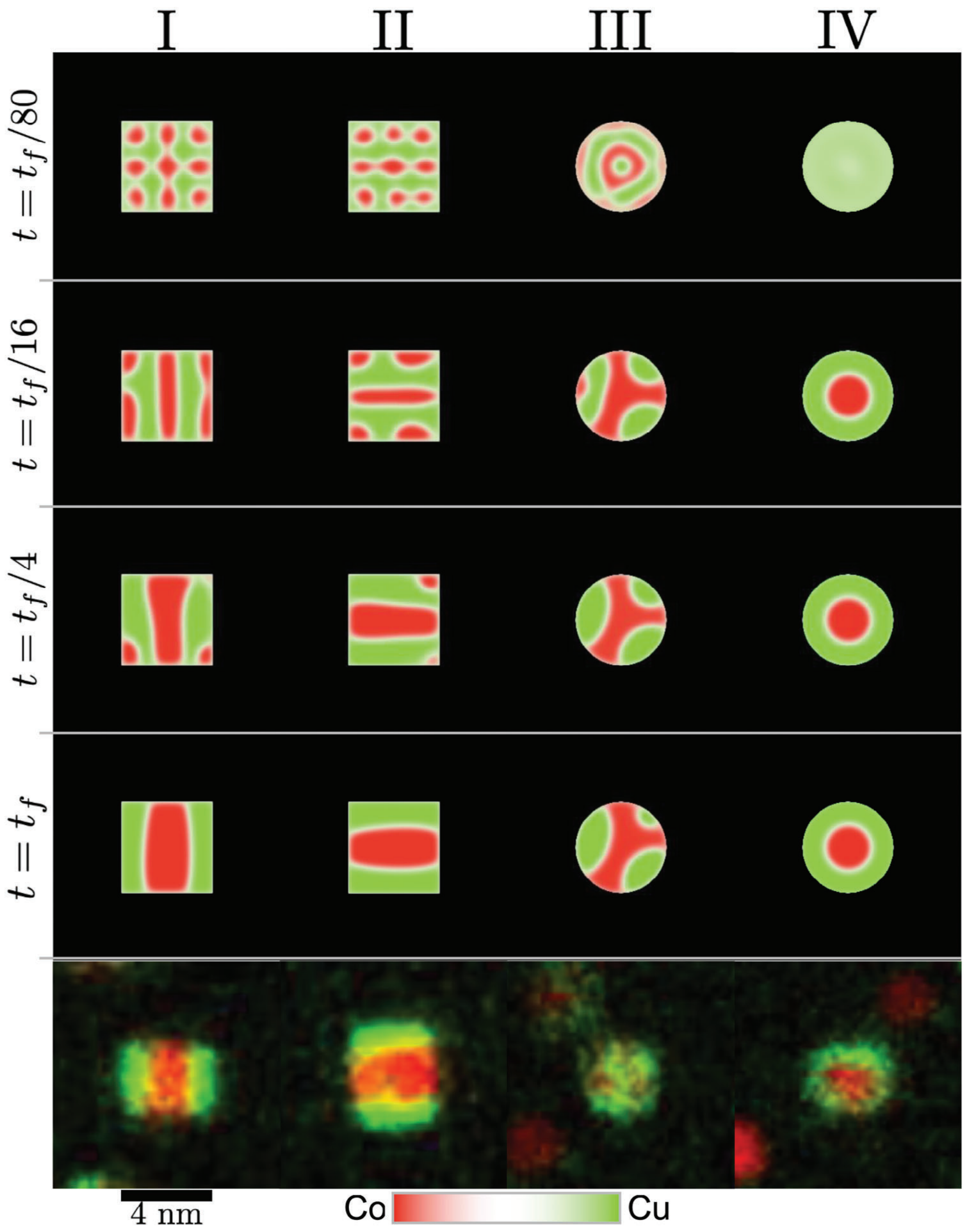

Figure 5. Microstructural evolution prediction of four Cu-Co nanopillars embedded in a BTO matrix for selected times: $t = t_f/80$, $t = t_f/16$, $t = t_f/4$, and $t = t_f$. The bottom row corresponds to the experimental observations. Each column corresponds to different initial conditions: I and II correspond to rectangular pillar morphologies; III is a cylindrical morphology, all three with an initial concentration $c_{\text{Cu},\circ} = 0.5$. IV corresponds to a cylindrical pillar morphology with $c_{\text{Cu},\circ} = 0.7$. The internal distribution of Co is a consequence of the interplay between surface segregation, chemical stresses, and the constraints imposed by the pillar morphology.

unique phase distribution based on different orientations of the interfaces.

Figure 5 shows a phase-field simulation directly comparing against the experimental micrographs (see Supporting Information for details on the model and numerical implementation, along with the videos).[37–39] Numerical simulations show that Co-rich regions form because the alloy composition displays that disfavors the formation of Co-Cu bonds, right in the middle of a spinodal decomposition regime.[40] This defines a critical wavelength for phase separation, $\lambda = 3.7$ nm, on par the diameter of the characteristic metallic pillar, $2\,r_p = 4$ nm. For short times, Cu segregates at the metal-ceramic interface, naturally defining Cu-rich regions at the center of the pillar. As phase separation progresses, smaller Cu-rich regions abutting the metal-ceramic interface shrink through mass transport along the pillar-ceramic interface.[41] Also, segregation at the corners of the rectangular cross-section pillar morphologies is energetically unfavored, rapidly dissolving to favor Co-rich regions at the center of the pillar. For those nanowires with an initial average composition of $c_{\text{Cu},\circ} = 0.5$, in Figure 5I and II (Co-Cu sandwiched structure in NP2 type), the pillars develop a layered internal morphology, in an attempt to enforce the contact angle energetics, ranging from 87.035° ± 0.932° to 103.01˚ ± 0.132°. In contrast, for $c_{\mathrm{Cu},^\circ} = 0.7$, the large excess free energy induced by Cu drives Co to the center of the pillar. This structure resembles the NP3 Co-Cu core–shell nanostructures in Figure 1. The stress and geometrical strain field distribution of four Cu-Co *n*anopillars embedded in a BTO matrix for long annealing times is also explored, as shown in Figure S9 (Supporting Information). Results demonstrate that chemomechanically-driven phase separation induces tensile stress in the Co-rich phase regions, which in turn is balanced by the surrounding, compressive Cu-rich regions. Co segregation in the pillar also attempts to minimize stress fields induced in the surrounding, crystallographically anisotropic BTO matrix. The corresponding geometrical strain field suggests that shear strain dominates deformation in the vicinity of the pillar-matrix interface, while the core of the pillars attempt to reach a hydrostatic state of strain.

Calculations demonstrate that the microstructural evolution of the Co-rich regions is controlled by the interplay between thermochemical,[38,40,42] chemomechanical,[43,44] and interfacial energy driving forces, as they interact with internal surfaces of the pillar morphology and the abutting BTO matrix. Internally, the local chemical potential gradients thermochemically phase-separate the two stable solute (or solvent) phases, in agreement with the phase diagram,[40,42] are instead dominated proportionally to the highest stress gradient, especially along phase boundaries, i.e., the direction of the first (largest) principal stress. This results in a large driving force for solute diffusion that not only minimizes the free energy of mixing but also attempts to minimize the elastic energy that is self-induced because of the composition-dependent lattice parameter. At the pillar-matrix interface, the self-induced mechanical and chemical equilibrium influences the resultant wetting angle of the phases. Overall, the VAN system will discourage the development of high elastic energy density regions, thus favoring to the formation of regions with minimized work of adhesion, i.e., with contact angles in the vicinity of 90± 15°. As a result, the morphology and dimensions of the pillar greatly influence the long-term internal microstructure of the nanopilars: A rectangular cross-section pillar defines internal lamellar structures for intermediate average Co-compositions, while a cylindrical pillar morphology results in a contact angle of ± 90°. The crystallographic anisotropy of the BTO matrix,[44,45] favors the formation of stresses outside the pillars which contribute to the local alignment of solute, particularly along elastically soft directions. Core–shell type nanopillar microstructures (NP3) are favored away from the $c_{\mathrm{Cu},^\circ} = 0.5$ composition, leading to Co-rich regions in hydrostatic tension, while the surrounding Cu-rich regions are in compression to balance out the state of stress of the overall structure.

3. ConclusionP

An oxide-metal nanocomposite thin film combining BTO with Co and Cu metals has been fabricated using a one-step pulsed laser deposition (PLD) method. The film exhibits a typical VAN structure characterized by metal NPs embedded in an oxide matrix, forming three distinct types of metal nanostructures: Co-rich NP1, Cu-sandwiched Co NP2 and Co-Cu core–shell NP3. Phase field modeling indicates the constructed structure is resulted from the interplay between thermochemical, chemomechanical, and interfacial energy driving forces. The BTO-CC film demonstrates remarkable properties, including SPR effect in the visible region induced by the non-noble Cu nanostructure, hyperbolic dispersion in the near-infrared region, and anisotropic optical and magnetic responses due to the film's anisotropic nature. Finally, the deposition of a BTO/BTO-CC bilayer confirms the ferroelectricity of the film, highlighting its potential as a new room-temperature multiferroic material.

4. Experimental Section

Target and Thin Film Preparation: The BTO-CC nanocomposite target was synthesized via conventional solid-state mixing, followed by spark plasma sintering (SPS) using a Thermal Technology 10–3 system at 200 °C and 30 MPa, with no holding time. The deposition of BTO-CC and BTO/BTO-CC thin films on STO (001) and 7 wt.% Nb-STO (001) substrates was performed using pulsed laser deposition (PLD) with a KrF excimer laser (Lambda Physik, $\lambda = 248$ nm). Prior to deposition, the chamber was evacuated to below 1×10^{-6} Torr. During deposition, the substrate temperature was maintained at 700 °C, with no oxygen flow into the chamber. The laser energy density was set at 2 J cm^{-2} and the deposition frequency at 5 Hz. For the deposition of the pure BTO layer, the substrate temperature was 700 °C with an oxygen pressure of 100 mTorr, and the laser energy density and frequency were adjusted to 1 J cm^{-2} and 2 Hz, respectively. After deposition, the sample was naturally cooled to room temperature.

Microstructure Characterization: X-ray diffraction (XRD) was conducted using a Panalytical X'Pert X-ray diffractometer. High-angle annular dark-field (HAADF) scanning transmission electron microscopy (STEM) images were acquired using an FEI Titan G2 80–200 microscope equipped with a Cs probe corrector. Additionally, a modified FEI Titan microscope, TEAM 0.5, featuring a high-brightness Schottky field emission electron source and an advanced hexapole-type illumination aberration corrector, was utilized for the imaging.

Magnetic Measurement: Magnetic hysteresis loops and magnetization-temperature curves were measured by a SQUID magnetometer (MPMS: Quantum Design). The magnetic field was employed either perpendicular (out-of-plane, OP) or parallel (in-plane, IP) to the film surface.

Optical Measurements: Transmittance spectra were acquired using UV–vis spectroscopy (Lambda 1050). Variable angle ellipsometry experiments were performed using a RC2 spectroscopic ellipsometer (J.A. Woollam Company). The ellipsometry measurements collected two parameters, Psi (φ) and Delta (Δ), which correspond to the ratio of the reflection coefficients for p-polarization r_p and s-polarization r_s light: $r_p/r_s = \tan(\varphi)\exp(i\Delta)$. By fitting the ellipsometry data with appropriate models, the effective refractive index and optical dielectric constants were determined. Angle-dependent and polarization-resolved reflectivity measurements were conducted at incident angles of 55°, 65°, and 75° to assess the reflectivity of the films.

Ferroelectric Measurements: Ferroelectric polarization-electric field (P-E) loop measurements were performed using a Precision LC II Ferroelectric Tester (Radiant Technologies, Inc.). Phase and amplitude maps were obtained with a conductive Pt-Ir coated Si tip (model: SCM-PIT V2) on a Bruker Dimension Icon Atomic Force Microscope (AFM).

Simulations: COMSOL Multiphysics Wave Optics Module with electromagnetic waves, frequency domain (ewfd) was applied for the optical simulation. Optical constants for Cu, Co, and BTO were directly taken from the software database and the simulated geometry was retrieved based on the plan-view and cross-sectional STEM images. Normal incidence depolarized electromagnetic field was applied with two ports on the top and bottom of the model. The details of the phase field modeling could be found in Supporting Information.

Supporting Information

Supporting Information is available from the Wiley Online Library or from the author.

Acknowledgements

The work was supported by the U.S. National Science Foundation (DMREF-2323752 for film growth and property characterizations, and DMR-2016453 for TEM characterization). J.H. acknowledges the support by the Shenzhen Science and Technology Program (JCYJ20210324133610028) and the Guangdong Basic and Applied Basic Research Foundation (2023A1515012594).

Conflict of Interest

The authors declare no conflict of interest.

Data Availability Statement

The data that support the findings of this study are available in the supplementary material of this article.

Keywords

anisotropic property, hyperbolic metamaterial, multiferroicity, plasmonic, vertically aligned nanocomposites (VANs)

Received: January 9, 2025
Revised: February 10, 2025
Published online:

---

[1] J. Huang, J. L. MacManus-Driscoll, H. Wang, *J. Mater. Res.* **2017**, *32*, 4054.
[2] J. L. MacManus-Driscoll, *Adv. Funct. Mater.* **2010**, *20*, 2035.
[3] J. Huang, W. Li, H. Yang, J. L. MacManus-Driscoll, *MRS Bull.* **2021**, *46*, 159.
[4] Z. Hu, J. Lu, H. Dou, J. Shen, J. P. Barnard, J. Liu, X. Zhang, H. Wang, *Nano Res.* **2024**, *17*, 3130.
[5] J. Song, D.i Zhang, P. Lu, H. Wang, X. Xu, M. L. Meyerson, S. G. Rosenberg, J. Deitz, J. Liu, X. Wang, X. Zhang, H. Wang, *Materials Today Nano* **2023**, *22*, 100316.
[6] O. Lee, S. A. Harrington, A. Kursumovic, E. Defay, H. Wang, Z. Bi, C.-F. Tsai, L. Yan, Q. Jia, J. L. MacManus-Driscoll, *Nano Lett.* **2012**, *12*, 4311.
[7] H. Zheng, F. Straub, Q. Zhan, P. L. Yang, W. K. Hsieh, F. Zavaliche, Y.-H. Chu, U. Dahmen, R. Ramesh, *Adv. Mater.* **2006**, *18*, 2747.
[8] J. Huang, L. Li, Z. Hu, B. K. Tsai, J. Huang, J. Shen, Y. Zhang, J. P. Barnard, J. Song, H. Wang, *Nano Lett.* **2024**, *24*, 10081.
[9] J. Huang, L. Li, P. Lu, Z. Qi, X. Sun, X. Zhang, H. Wang, *Nanoscale* **2017**, *9*, 7970.
[10] G. Wang, F. Sun, S. Zhou, Y. Zhang, F. Zhang, H. Wang, J. Huang, Y. Zheng, *ACS Appl. Mater. Interfaces* **2024**, *16*, 12073.
[11] S. Misra, H. Wang, *Mater. Horiz.* **2021**, *8*, 869.
[12] J. Huang, H. Wang, Z. Qi, P. Lu, D. Zhang, B. Zhang, Z. He, H. Wang, *Nano Lett.* **2021**, *21*, 1032.
[13] J. Wang, X. Ning, Z. Gao, J. Wang, X. San, S. Wang, *Acta Mater.* **2022**, *227*, 117692.
[14] J. Huang, Y. Fang, P. Lu, J. Lu, H. Wang, *Nano Res.* **2024**, *17*, 8226.
[15] R. Wu, D. Zhang, T. Maity, P. Lu, J. Yang, X. Gao, S. Zhao, X. Wei, H. Zeng, A. Kursumovic, G. Tian, W. Li, C. Yun, Y. Wang, Z. Ren, Z. Zhou, M. Liu, K. H. L. Zhang, Q. Jia, J. Yang, H. Wang, J. L. MacManus-Driscoll, *Nat. Electron.* **2021**, *4*, 333.
[16] J. Huang, X. Phuah, L. McClintock, P. Padmanabhan, K. Vikrant, H. Wang, D. Zhang, H. Wang, P. Lu, X. Gao, X. Sun, X. Xu, R. García, H. Chen, X. Zhang, H. Wang, *Mater. Today* **2021**, *51*, 39.
[17] M. Hennes, E. Fonda, N. Casaretto, J. Buchwald, X. Weng, G. Patriarche, D. Demaille, Y. Zheng, F. Vidal, *Phys. Rev. Materials* **2020**, *4*, 126001.
[18] J. Song, D. Zhang, P. Lu, Y. Zhang, H. Wang, H. Dou, X. Xu, J. Deitz, X. Zhang, H. Wang, *ACS Appl. Mater. Interfaces* **2023**, *15*, 37810.
[19] S. Misra, L. Li, D. Zhang, J. Jian, Z. Qi, M. Fan, H. Chen, X. Zhang, H. Wang, *Adv. Mater.* **2019**, *31*, 1806529.
[20] X. Wang, J. Jian, H. Wang, J. Liu, Y. Pachaury, P. Lu, B. X. Rutherford, X. Gao, X. Xu, A. El-Azab, X. Zhang, H. Wang, *Small* **2021**, *17*, 2007222.
[21] J. Huang, Z. Qi, L. Li, H. Wang, S. Xue, B. Zhang, X. Zhang, H. Wang, *Nanoscale* **2018**, *10*, 17182.
[22] Y. Zhang, D. Zhang, J. Liu, P. Lu, J. Deitz, J. Shen, Z. He, X. Zhang, H. Wang, *Nanoscale* **2022**, *14*, 11979.
[23] X. Weng, M. Hennes, A. Coati, A. Vlad, Y. Garreau, M. Sauvage-Simkin, E. Fonda, G. Patriarche, D. Demaille, F. Vidal, Y. Zheng, *Phys. Rev. Materials* **2018**, *2*, 106003.
[24] J. Huang, X. Wang, X. Phuah, P. Lu, Z. Qi, H. Wang, *Materials Today Nano* **2019**, *8*, 100052.
[25] F. J. Bonilla, A. Novikova, F. Vidal, Y. Zheng, E. Fonda, D. Demaille, V. Schuler, A. Coati, A. Vlad, Y. Garreau, M. S. Simkin, Y. Dumont, S. Hidki, V. Etgens, *ACS Nano* **2013**, *7*, 4022.
[26] R. L. Paldi, X. Wang, X. Sun, Z. He, Z. Qi, X. Zhang, H. Wang, *Nano Lett.* **2020**, *20*, 3778.
[27] G. H. Chan, J. Zhao, E. M. Hicks, G. C. Schatz, R. P. Van Duyne, *Nano Lett.* **2007**, *7*, 1947.
[28] Y. Xin, K. Yu, L. Zhang, Y. Yang, H. Yuan, H. Li, L. Wang, J. Zeng, *Adv. Mater.* **2021**, *33*, 2008145.
[29] G. Radtke, M. Hennes, M. Bugnet, Q. M. Ramasse, X. Weng, D. Demaille, B. Gobaut, P. Ohresser, E. Otero, F. Choueikani, A. Juhin, P. Sainctavit, Y. Zheng, F. Vidal, *Adv. Mater. Interfaces* **2019**, *6*, 1900549.
[30] Y. F. Zhukovskii, E. A. Kotomin, D. E. Ellis, *phys. stat. sol. (b)* **2008**, *245*, 980.
[31] G. Radaelli, D. Petti, E. Plekhanov, I. Fina, P. Torelli, B. R. Salles, M. Cantoni, C. Rinaldi, D. Gutierrez, G. Panaccione, M. Varela, S. Picozzi, J. Fontcuberta, R. Bertacco, *Nat. Commun.* **2014**, *5*, 3404.
[32] A. R. Indhu, C. Dharanya, G. Dharmalingam, *Plasmonics* **2024**, *19*, 1303.
[33] M. Braik, I. Sow, J. Nelayah, A. Belkhir, M. Faustini, S. Mercone, S. Nowak, P. Decorse, J.-Y. Piquemal, N. Felidj, *Nanoscale* **2021**, *13*, 2639.
[34] K. L. Kelly, E. Coronado, L. Zhao, G. C. Schatz, *J. Phys. Chem. B* **2003**, *107*, 668.
[35] L. Novotny, B. Hecht, *Principles of nano-optics*, 2nd ed., Cambridge University Press, Cambridge, New york **2012**.
[36] G. Han, B. Zong, P. Luo, Y. Wu, *J. Appl. Phys.* **2003**, *93*, 9202.
[37] O. Redlich, A. T. Kister, *Ind. Eng. Chem.* **1948**, *40*, 345.
[38] G. Giudicelli, A. Lindsay, L. Harbour, C. Icenhour, M. Li, J. E. Hansel, P. German, P. Behne, O. Marin, R. H. Stogner, J. M. Miller, D. Schwen, Y. Wang, L. Munday, S. Schunert, B. W. Spencer, D. Yushu, A. Recuero, Z. M. Prince, M. Nezdyur, T. Hu, Y. Miao, Y. S. Jung, C. Matthews, A. Novak, B. Langley, T. Truster, N. Nobre, B. Alger, D. Andrs, et al., *SoftwareX* **2024**, *26*, 101690.
[39] W. J. Boettinger, J. A. Warren, C. Beckermann, A. Karma, *Annu. Rev. Mater. Res.* **2002**, *32*, 163.
[40] J. Kubišta, J. Vřešťál, *J. Phase Equilib.* **2000**, *20*, 125.
[41] S. J. Rothman, N. L. Peterson, *Physica Status Solidi B* **1969**, *35*, 305.

[42] J. Lund, H. Wang, R. D. Braatz, R. E. García, *Mater. Adv.* **2022**, *3*, 8485.

[43] L. E. Malvern, *Introduction to the Mechanics of Continuous Medium*, Prentice-Hall, Inc, New Jersey **1969**, 154.

[44] *The Materials Project, Materials Data on Cu (SG:225) by Materials Project*, The United States, United States, **2020**.

[45] F. Jona, G. Shirane, *Ferroelectric Crystals*, Dover Publications, New York **1993**.